

Gravitational waves for eccentric extreme mass ratio inspirals of self-dual spacetime

Yunlong Liu and Xiangdong Zhang^a

Department of Physics, South China University of Technology, Guangzhou 510641, China

In this paper, we calculate the frequencies of geodesic orbits in self-dual spacetime on the equatorial plane and obtain the leading-order effects of loop quantum parameters P on the energy flux and angular momentum flux in eccentric extreme mass ratio inspirals. The gravitational waveform under different eccentricity is carried out by improved “analytic-kludge” method. Through the calculation of waveform mismatches for the LISA detector, the constraints on loop quantum parameters will be improved by 1 to 2 orders of magnitude, compared to the weak field experiments in the solar system, and can reach the level of 10^{-8} .

I. INTRODUCTION

General relativity (GR) has been developed for over a century, and so far the observed data have not exceeded the predictions of general relativity. However, there are irreconcilable problems between GR and quantum mechanics (QM). Hence, establishing a unified theory of GR and QM is the primary task in theoretical physics. Today, various quantum gravity theories have been proposed. Among them, loop quantum gravity (LQG) is notable due to its background independence and non-perturbative nature [1–4].

The application of LQG to cosmology, known as loop quantum cosmology (LQC), now becomes a fruitful field. The most notable feature of LQC is that it successfully uses the “Big Bounce” to replace the classical big bang singularity [5–10].

Due to the success of LQC, and note that the interior of Schwarzschild black hole is isometric to the Kantowski-Sachs model [7, 11], the attempt to apply quantization techniques to black holes to address the issue of black hole singularity is a very intriguing idea. By utilizing the techniques developed in LQC and through different quantization schemes, various LQG black hole models can be constructed [12]. Among these different models, one famous and well studied method is to set the loop quantum regularization parameters as constants [7, 13]. By using the technique of holonomy correction, a so-called self-dual solution of loop quantum black holes without curvature singularities has been constructed [14, 15].

One natural question for a quantum black hole model is that does LQG parameters can generate any observable features, or whether these quantum parameters can be constrained through current or future experiments and observations? A lot of effects have been made towards this direction. For example, in the solar system [16], or in strong field regimes observations of binary pulsars [17–19], imaging of black hole shadows [20, 21], and direct detection of gravitational wave (GW) [22]. Based on this, lots of properties and observational constraints in self-dual spacetimes have been studied [23–26]. As a result, the best constraints on LQG parameters are provided within the solar system experiments [24], with a limit of quantum parameter $|\delta| < 0.0199$ (or $P < 5.5 \times 10^{-6}$).

To obtain with more tighter constraints on parameters, more precise experimental tests are necessary. The detection of GWs presents an opportunity for this. The next generation of space-based detectors, such as LISA [27], Tianqin [28], and Taiji [29, 30], will expand the types and spectra of GW signals to unprecedented precision, providing possibilities to testing LQG and constrain the quantum parameters.

Among various GW signals, an important one comes from the extreme mass ratio inspiral (EMRI) system composed of a massive black hole ($M \approx 10^{5\sim 7} M_{\odot}$) and a small compact object ($m \approx 10^{0\sim 2} M_{\odot}$) [31]. Analyzing EMRIs requires the establishment of corresponding waveform models [32–37]. For example, the high-precision kludge method [33] has been proposed. However, these methods come with a high computational cost. To save computational resources, Barack and Cutler [32] proposed the “analytic kludge” (AK) model. This model can quickly obtain a GW template of EMRI, and can reflect the main physical properties of the real EMRI waveform [33]. However, when this method approaches the innermost stable orbit (ISO), the phase error will increase rapidly. In order to solve this problem, Chua et al. proposed an improved AK waveform method [34, 35] with “map” way, and obtained more accurate waveforms.

In this paper, we propose a new improvement on the AK method differs from the “map” way of Chua [34, 35]. We used the inverse series way and obtain the high precision perihelion precession angle, which encodes the major cumulative orbital error in spherically symmetric spacetime when energy and angular momentum fluxes of GWs are not considered. As a result, we calculate the impact of LQG parameter on GWs and explore the detection capabilities of space-based GW detectors for the parameter of LQG. We find that the constraint ability on loop quantum parameters will be greatly improved compared with the experiments in the solar system.

^a Corresponding author. scxdzhang@scut.edu.cn

The structure of this paper is as follows: In Sec. II, we introduce the geodesic equations on the self-dual spacetime and calculate two mean orbital frequencies on the equatorial plane, and give the leading-order correction of fluxes due to the LQG effects. In Sec. III, we provide two improved adiabatic evolution equations for orbitals and also present the quadrupole moment waveform in the self-dual spacetime. Then, in Sec. IV, we obtain the numerical solutions of ODEs from the previous section and corresponding gravitational waveforms. With all this, we analyze the detection capability of LISA for the parameter of LQG with mismatch in Sec. V. Finally, the conclusions and perspectives are provided in Sec. VI.

II. THE BACKGROUND METRIC AND MOTION EQUATION

A. background metric

The metric of static spherically symmetric self-dual black hole is given by[12, 15]:

$$ds^2 = -A(r)dt^2 + B(r)dr^2 + D(r)d\Omega^2, \quad (1)$$

where

$$A(r) = \frac{(r - r_+)(r - r_-)(r - r_*)}{r^4 + a_0^2}, \quad (2)$$

$$B(r) = \frac{(r + r_+)^2 (r^4 + a_0^2)}{(r - r_+)(r - r_-)r^4}, \quad (3)$$

$$D(r) = r^2 + \frac{a_0^2}{r^2}. \quad (4)$$

Here, $r_+ = 2M/(1+P)^2$, $r_- = 2MP^2/(1+P)^2$, and $r_* = \sqrt{r_+r_-}$. It should be noted that a_0 depends on the minimal area element Δ and P corresponds to the regularization parameter δ in LQG as

$$a_0 = \frac{\Delta}{8\pi}; \quad P = \frac{\sqrt{1 + \gamma^2 \delta^2} - 1}{\sqrt{1 + \gamma^2 \delta^2} + 1}; \quad (5)$$

When $a_0 = 0$ and $P = 0$, the spacetime can return to the Schwarzschild case. Since the parameter a_0 usually appears at higher order terms in the Taylor series expansion while the gravitational wave we concern in this paper only involves quadrupole which is irrelevant with higher order terms and hence we can safely set $a_0 = 0$ in the following. Moreover, we adopt geometric units $G = c = 1$.

B. Equations of motion in the spherically symmetric metric

Now we turn to the equations of motion. By using the Killing vectors, we can define two conserved quantities, energy E and angular momentum L as

$$E := mA(r)\frac{dt}{d\tau}, \quad (6)$$

$$L := m\sin^2(\theta)D(r)\frac{d\phi}{d\tau}. \quad (7)$$

Through the Lagrangian and separating variables, we can obtain the equations of motion of this spacetime as follows:

$$\frac{dt}{d\tau} = \frac{E}{mA(r)}, \quad (8)$$

$$\left(\frac{dr}{d\tau}\right)^2 = \frac{B(r)}{D(r)} \left(-D(r) + \frac{D(r)}{A(r)} \frac{E^2}{m^2} - \frac{C}{m^2}\right), \quad (9)$$

$$\left(\frac{d\theta}{d\tau}\right)^2 = \frac{C}{m^2} - \frac{L^2}{m^2 \sin^2(\theta)}, \quad (10)$$

$$\frac{d\phi}{d\tau} = \frac{L}{m \sin^2(\theta) D(r)}. \quad (11)$$

Moreover, to facilitate calculations, we perform a variable transformation from the original coordinate system (t, r, θ, ϕ) to the new one (t, ψ, θ, ϕ) , where

$$r(\psi) = \frac{Mp}{1 + e \cos(\psi)}, \quad (12)$$

where p is the dimensionless semilatus rectum and e is the eccentricity.

Note that the distances of the orbit's pericenter and apocenter are respectively given by:

$$r_{\text{apo}} = \frac{Mp}{1 - e}, \quad (13)$$

$$r_{\text{peri}} = \frac{Mp}{1 + e}. \quad (14)$$

For $0 < e < 1$, the radial velocity of the small body equal zero ($dr/d\tau = 0$) at the pericenter or apocenter, where $\psi = \mathbb{N}\pi$, $\mathbb{N} = 1, 2, 3, \dots$. Hence, $dr/d\tau$ and $\sin(\psi)$ change sign on $\psi = \mathbb{N}\pi$ at the same time. Take the derivative of Eq. (12), we get

$$\frac{d\psi}{d\tau} = \frac{(1 + e \cos(\psi))^2}{eMp} \frac{1}{\sin(\psi)} \frac{dr}{d\tau}. \quad (15)$$

Therefore, $d\psi/d\tau$ always retains the same sign. This feature enables us to set $d\psi/d\tau \geq 0$ which indicates ψ monotonically increases with proper time τ . For equatorial plane orbits, we have $\theta = \pi/2$ and $d\theta/d\tau = 0$. From Eq. (10), we have $C = L^2$. The equations of motion can be reduced to:

$$\frac{dt}{d\tau} = \frac{E}{mA(r(\psi))}, \quad (16)$$

$$\frac{d\psi}{d\tau} = \frac{(1 + e \cos(\psi))^2}{eMp\sqrt{\sin(\psi)^2}} \sqrt{\frac{1}{B(r(\psi))} \left(-1 + \frac{1}{A(r(\psi))} \frac{E^2}{m^2} - \frac{1}{D(r(\psi))} \frac{L^2}{m^2}\right)}, \quad (17)$$

$$\frac{d\theta}{d\tau} = 0, \quad (18)$$

$$\frac{d\phi}{d\tau} = \frac{L}{mD(r(\psi))}. \quad (19)$$

Next, let's further analyze the relationship between (p, e) and (E, L) . Since we have $dr/d\tau = 0$ at r_{apo} and r_{peri} , we can obtain the relationship between (p, e) and (E, L) from Eq. (10) as follows:

$$E = \frac{m\sqrt{A(r_{\text{apo}})}\sqrt{A(r_{\text{peri}})}\sqrt{D(r_{\text{apo}}) - D(r_{\text{peri}})}}{\sqrt{A(r_{\text{peri}})D(r_{\text{apo}}) - A(r_{\text{apo}})D(r_{\text{peri}})}}, \quad (20)$$

$$L = \frac{m\sqrt{A(r_{\text{apo}}) - A(r_{\text{peri}})}\sqrt{D(r_{\text{apo}})}\sqrt{D(r_{\text{peri}})}}{\sqrt{A(r_{\text{peri}})D(r_{\text{apo}}) - A(r_{\text{apo}})D(r_{\text{peri}})}}. \quad (21)$$

It should be note that when $e = 0$, Eqs. (15) and (17) are not valid, but we can do a similar analysis. Since in this

case, we have $dr/d\tau = 0$, $dr^2/d\tau^2 = 0$ and $r_{\text{apo}} = r_{\text{peri}} = Mp$, hence we can obtain:

$$E = \frac{mA[r_{\text{apo}}] \sqrt{D'[r_{\text{apo}}]}}{\sqrt{-D[r_{\text{apo}}]A'[r_{\text{apo}}] + A[r_{\text{apo}}]D'[r_{\text{apo}}]}}, \quad (22)$$

$$L = \frac{mD[r_{\text{apo}}] \sqrt{A'[r_{\text{apo}}]}}{\sqrt{-D[r_{\text{apo}}]A'[r_{\text{apo}}] + A[r_{\text{apo}}]D'[r_{\text{apo}}]}}. \quad (23)$$

Expanding the energy E and angular momentum L in terms of the dimensionless semilatus rectum p , we have:

$$\frac{E}{m} = 1 + \frac{(-1 + e^2)(1 - P)^2}{2(1 + P)^2 p} + \frac{3(-1 + e^2)^2(1 - P)^4}{8(1 + P)^4 p^2} + \mathcal{O}(p^{-3}), \quad (24)$$

$$\frac{L}{Mm} = \frac{1 - P}{1 + P} p^{1/2} - \frac{3 + e^2(1 - P)^4 - 4P + 10P^2 - 4P^3 + 3P^4}{2(1 - P)(1 + P)^3} p^{-1/2} + \mathcal{O}(p^{-3/2}). \quad (25)$$

It is easy to see that when $P = 0$, the above result reduced to the Schwarzschild case, while $e = 0$, the case of circular orbit will be recovered.

C. Orbital frequencies

We assume that the trajectory is on the equatorial plane $\theta = \pi/2$, it means that the polar angle frequency Ω_θ can be neglected. For bounded orbits, we are left with two frequencies Ω_r and Ω_ϕ that correspond to the parameters $r(\psi)$ and ϕ . The coordinate time spent by the test body in moving from one pericenter to the next one is given by [38]:

$$\Lambda_t = \int_0^{t_0} dt = \int_0^{2\pi} \frac{dt}{d\psi} d\psi. \quad (26)$$

The corresponding change in the azimuthal angle ϕ reads:

$$\Lambda_\phi = \int_0^{\phi_0} d\phi = \int_0^{2\pi} \frac{d\phi}{d\psi} d\psi. \quad (27)$$

For this, the average angular velocity of $r(\psi)$ and ϕ over each period can be expressed as

$$\Omega_r = \frac{2\pi}{\Lambda_t}; \quad \Omega_\phi = \frac{\Lambda_\phi}{\Lambda_t}. \quad (28)$$

By combining the geodesic equations (16) and (19), we can obtain the following expansion:

$$\begin{aligned} \Omega_\phi &= \frac{(1 - P)X^{3/2}}{(1 + P)Mp^{3/2}} - \frac{X^{3/2}}{(1 - P)(1 + P)^3 Mp^{5/2}} \\ &\times \left(-3 + 4P - 6P^2 + 4P^3 - 3P^4 + (3 - 8P + 10P^2 - 8P^3 + 3P^4)X \right) \\ &- \frac{X^{3/2}}{4(1 - P)^3(1 + P)^5 Mp^{7/2}} \left(-57 - 4(1 - P)^4 X^2 (3 + \mathcal{P}_2)^2 \right. \\ &\left. + 2(1 - P)^4 X^{3/2} (15 + \mathcal{P}_4) + (1 - P)^2 X (63 + \mathcal{P}_6) + \mathcal{P}_8 \right) + \mathcal{O}(p^{-9/2}), \end{aligned} \quad (29)$$

$$\begin{aligned} \Omega_r &= \frac{(1 - P)X^{3/2}}{(1 + P)Mp^{3/2}} - \frac{(1 - P)X^{5/2}(3 + \mathcal{P}_2)}{(1 + P)^3 Mp^{5/2}} \\ &- \frac{(1 - P)X^{5/2}}{2(1 + P)^5 Mp^{7/2}} \left(12(1 + 3P^2 + P^4) - 2X(3 + \mathcal{P}_2)^2 + X^{1/2}(15 + \mathcal{P}_4) \right) + \mathcal{O}(p^{-9/2}), \end{aligned} \quad (30)$$

where

$$\mathcal{P}_2 = -2P + 3P^2, \quad (31)$$

$$\mathcal{P}_4 = -12P + 26P^2 - 12P^3 + 15P^4, \quad (32)$$

$$\mathcal{P}_6 = -122P + 233P^2 - 284P^3 + 233P^4 - 122P^5 + 63P^6, \quad (33)$$

$$\mathcal{P}_8 = 200P - 364P^2 + 568P^3 - 662P^4 + 568P^5 - 364P^6 + 200P^7 - 57P^8. \quad (34)$$

Thus, we can obtain the frequency of perihelion precession $\dot{\hat{\gamma}}$ as:

$$\begin{aligned} \dot{\hat{\gamma}} = & \frac{(-3 + 4P - 6P^2 + 4P^3 - 3P^4)X^{3/2} - (1 - P)(2P - 5P^2 + 3P^3 + (1 - P)\mathcal{P}_2)X^{5/2}}{- (1 - P)(1 + P)^3 M p^{5/2}} \\ & + \frac{X^{5/2}(-24(1 - P)^4(1 + 3P^2 + P^4) + (1 - P)^2(63 + \mathcal{P}_6)) + X^{3/2}(-57 + \mathcal{P}_8)}{-4(1 - P)^3(1 + P)^5 M p^{7/2}} + \mathcal{O}(p^{-9/2}), \end{aligned} \quad (35)$$

where $X = 1 - e^2$. Here, it can be easily verified that when $P = 0$, the result returns to the Schwarzschild case. In our code, in order to obtain a higher precision geodesic orbit, we use a higher order series expansion formula of $\dot{\hat{\gamma}}$. However, due to the increased complexity, we will not show it here.

D. Fluxes

In the AK waveform on the equatorial plane, in addition to the two motion equations obtained from geodesics, there are also adiabatic evolution for frequency ν and eccentricity e caused by energy and angular momentum flux of GW.

We use the quadrupole approximation to calculate the energy flux and angular momentum flux[39, 40] as

$$\frac{dE}{dt} = \frac{1}{5} \langle \ddot{Q}_{ij} \ddot{Q}_{ij} \rangle, \quad (36)$$

$$\frac{dL^i}{dt} = \frac{2}{5} \epsilon^{ikl} \langle \ddot{Q}_{ka} \ddot{Q}_{la} \rangle, \quad (37)$$

where the quadrupole moment \mathcal{Q} can be described in terms of the mass moment \mathcal{M} as follows:

$$\mathcal{Q}^{ij} = \mathcal{M}^{ij} - \frac{1}{3} \delta^{ij} \mathcal{M}_{kk}, \quad (38)$$

$$\mathcal{M}^{ij} = \int d^3x T^{00}(t, \mathbf{x}) x^i x^j, \quad (39)$$

where T^{ab} is the stress-energy tensor and \mathbf{x} is the position vector. In the point particle approximation and in the center-of-mass coordinates, the second mass moment can be expressed as:

$$\mathcal{M}^{ij} = \mu x_0^i x_0^j, \quad (40)$$

where $\mu = mM/(m + M)$ is the reduced mass, and \mathbf{x}_0 is the relative position between the small body and the central black hole. In the weak field approximation, $x_0^i = (r \cos \phi, r \sin \phi, 0)$, the leading-order energy flux and angular momentum flux are given as follows:

$$\frac{1}{m} \frac{dE}{dt} = - \frac{(1 - e^2)^{3/2} (96 + 292e^2 + 37e^4) (-1 + P)^6 \mu^2}{15(1 + P)^6 M^2 m p^5} + \mathcal{O}(p^{-6}), \quad (41)$$

$$\frac{1}{mM} \frac{dL}{dt} = - \frac{4(1 - e^2)^{3/2} (8 + 7e^2) (1 - P)^5 \mu^2}{5(1 + P)^5 M^2 m p^{7/2}} + \mathcal{O}(p^{-9/2}). \quad (42)$$

III. ORBITAL EVOLUTION EQUATIONS

Now we have the expressions for energy flux and angular momentum flux in terms of a series expansion in Eq.(41)-(42), the next step is to convert this series expansion in terms of the Keplerian frequency ν . Additionally, in equations

(29) and (30), there are two frequencies involved, Ω_r and Ω_ϕ . In the conventional approach of the *AK* method, it is usually assumed that $\Omega_r \approx 2\pi\nu$ [34, 35]. However, this approximation introduces significant errors, especially when approaching the innermost stable orbit (ISO) [34, 35]. A detailed comparison of Ω_r , Ω_ϕ and $2\pi\nu$ is provided in Appendix A 1. Since this paper only considers the spherically symmetric case, we do not use the “map” method proposed in [34] to address the large discrepancies between the orbital and precession frequency $\{f_{orb}, f_{peri}\}$ and the approximations of $\{\Omega_r/2\pi, (\Omega_\phi - \Omega_r)/2\pi\}$. Instead, we will directly employ higher order series expansions of $\dot{\hat{\gamma}}$ to resolve this issue.

A. Geodesic Equations

In this part, we will use both frequencies, $\Omega_r = 2\pi\nu_r$ and $\Omega_\phi = 2\pi\nu_\phi$, as base frequencies to obtain the approximate equations of geodesics.

1. The large eccentricity method (*eL* method)

We assume $\Omega_r = 2\pi\nu_r$, and by calculating the inverse series expansion of Eq. (29), we obtain the relationship between p and the radial frequency ν_r :

$$\begin{aligned} p = & \left(\frac{1-P}{1+P}\right)^{2/3} \frac{X}{(2\pi M\nu_r)^{2/3}} - \frac{2(3+P(-2+3P))X}{3(1+P)^2} \\ & + (2\pi M\nu_r)^{2/3} \left(\frac{1+P}{1-P}\right)^{2/3} \frac{1}{9(1+P)^4} \left(-36(1+3P^2+P^4)\right. \\ & \left.+ 3(-15+12P-26P^2+12P^3-15P^4)\sqrt{X} + (3-2P+3P^2)^2 X\right) + \mathcal{O}((2\pi M\nu_r)^{4/3}). \end{aligned} \quad (43)$$

If we substitute Eq. (43) into Eq. (29), we can obtain $\Omega_r = 2\pi\nu_r + \mathcal{O}(\nu_r^{7/3})$. By substituting the expression (43) into Eq. (35), evolution equation determined by geodesic is given by

$$\frac{d\Psi}{dt} = \Omega_r = 2\pi\nu_r, \quad (44)$$

$$\frac{d\Phi}{dt} = \Omega_r + \frac{d\hat{\gamma}}{dt}, \quad (45)$$

$$\begin{aligned} \frac{d\hat{\gamma}}{dt} = & \frac{(1+P^2)(3-4P+3P^2)(2\pi M\nu_r)^{5/3}}{(1-P)^{8/3}(1+P)^{4/3}} \frac{(2\pi M\nu_r)^{5/3}}{(1-e^2)M} \\ & + \frac{1}{(1-P)^{16/3}(1+P)^{8/3}} \frac{(2\pi M\nu_r)^{7/3}}{12M(1-e^2)^2} \left(2(117 + \mathcal{P}_{2\gamma 0}^8) - e^2(63 + \mathcal{P}_{\gamma 2}^8)\right) + \mathcal{O}((2\pi M\nu_r)^3), \end{aligned} \quad (46)$$

where Ψ represents mean anomaly for ψ and Φ denotes mean “longitude” for ϕ with

$$\mathcal{P}_{2\gamma 0}^8 = -432P + 860P^2 - 1360P^3 + 1582P^4 - 1360P^5 + 860P^6 - 432P^7 + 117P^8, \quad (47)$$

$$\mathcal{P}_{\gamma 2}^8 = (7-6P+7P^2)(3-5P+5P^2-3P^3)^2 - 63. \quad (48)$$

2. The small eccentricity method (*eS* method)

Analogously, we set $\Omega_\phi = 2\pi\nu_\phi$. By computing the inverse series of Eq. (30), we can obtain the relation between p and the “longitude” frequency ν_ϕ :

$$\begin{aligned} p = & \left(\frac{1-P}{1+P}\right)^{2/3} \frac{X}{(2\pi M\nu_\phi)^{2/3}} - \frac{2(3+P(-2+3P))X}{3(1+P)^2} + \frac{2(1+P^2)(3+P(-4+3P))}{3(-1+P^2)^2} \\ & + F[P, X](2\pi M\nu_\phi)^{2/3} + \mathcal{O}((2\pi M\nu_\phi)^{4/3}). \end{aligned} \quad (49)$$

Here,

$$F[P, X] = \frac{(1-P)^{10/3}}{9(1+P)^{10/3}} \left((81 - 360P + 572P^2 - 984P^3 + 1126P^4 - 984P^5 + 572P^6 - 360P^7 + 81P^8)X^{-1} + \right. \\ \left. (-9 + 6P + P^2 + 132P^3 + P^4 + 6P^5 - 9P^6)(1-P)^2 \right. \\ \left. - 6(15 - 12P + 26P^2 - 12P^3 + 15P^4)(1-P)^4\sqrt{X} + 2(3 - 2P + 3P^2)^2(1-P)^4X \right). \quad (50)$$

Substituting Eq.(49) into Eq. (30), we get $\Omega_\phi = 2\pi\nu_\phi + \mathcal{O}(\nu_\phi^{7/3})$. By plugging the Eq. (49) into Eq. (35), equations of motion can be obtained as

$$\frac{d\Psi}{dt} = \Omega_r = \Omega_\phi - \frac{d\hat{\gamma}}{dt}, \quad (51)$$

$$\frac{d\Phi}{dt} = \Omega_\phi = 2\pi\nu_\phi, \quad (52)$$

$$\frac{d\hat{\gamma}}{dt} = -\frac{(1+P^2)(3-4P+3P^2)(2\pi M\nu_\phi)^{5/3}}{(1-P)^{8/3}(1+P)^{4/3}(1-e^2)M} \\ - \frac{1}{(1-P)^{16/3}(1+P)^{8/3}} \frac{(2\pi M\nu_\phi)^{7/3}}{12M(1-e^2)^2} (2(27 + \mathcal{P}_{1\gamma 0}^8) - e^2(63 + \mathcal{P}_{\gamma 2}^8)) + \mathcal{O}((2\pi M\nu_r)^3), \quad (53)$$

where

$$\mathcal{P}_{1\gamma 0}^8 = -192P + 340P^2 - 640P^3 + 722P^4 - 640P^5 + 340P^6 - 192P^7 + 27P^8. \quad (54)$$

Along these lines, we can extend the approximate Eq. (46) or Eq. (53) to higher orders. In the following part of the paper, whenever we talk about using Eq. (46) or Eq. (53) up to (n, m) orders, it means that the approximation of $d\hat{\gamma}/dt$ will be calculated to n -th orders ($\mathcal{O}((2\pi M\nu_\kappa)^{(2n+3)/3})$, $\kappa = r, \phi$) in Schwarzschild part and m -th orders in LQG part. For example, the expressions in Eq. (46) or Eq.(53) is up to $(2, 2)$ orders.

3. Orbits

As the extreme mass ratio parameter m/M approaches zero, the energy and angular momentum flux also tend to zero, and the orbit can be described by a timelike geodesic and the information of orbit is completely encoded in the Eqs. (44)-(46) or (51)-(53). However, the azimuthal angle Ψ and Φ are the mean of true angle ψ and ϕ . The relationship between the true anomaly ψ and the mean anomaly Ψ can be derived using classical methods, and it is as follows[40]:

$$\psi \approx \psi_{Ap} = 2 \arctan \left(\left(\frac{1+e}{1-e} \right)^{1/2} \tan \left(\frac{u}{2} \right) \right) + 2\pi \text{IntegerPart} \left(\frac{\Psi + \pi}{2\pi} \right), \quad (55)$$

$$u = \Psi + e \sin(u). \quad (56)$$

The third order approximation for u is:

$$u = \Psi + e \sin(\Psi + e \sin((\Psi + e \sin(\Psi)))). \quad (57)$$

Moreover, ϕ can be approximated as:

$$\phi \approx \phi_{Ap} = \psi_{Ap} \left(1 + \frac{\hat{\gamma}}{\Psi} \right). \quad (58)$$

The approximate orbit is given by $r^i = (r \cos(\phi), r \sin(\phi), 0)$, where r is defined in Eq. (12). In Eq. (58), the use of the mean precession angle $\hat{\gamma}$ and mean anomaly Ψ introduces periodic errors in the orbit. In addition, from Eqs. (44) - (46) or (51) - (53), we know that the main and cumulative error is mainly in $\hat{\gamma}$. Hence, the analysis of the error of $\hat{\gamma}$ is helpful for us to estimate the orbit accuracy which will be shown in Appendix A 2.

Note that, to reduce this error accumulates over time, we usually employing higher orders of $d\hat{\gamma}/dt$ in Eq. (53) or (46) when calculating numerical solutions. By numerically solving the system of Eqs. (16)-(19), Eqs. (44)-(46) up to

(10, 5) orders, or Eqs. (51) -(53) up to (11, 6) orders, we obtain the following orbital results as shown in the Fig. 1:

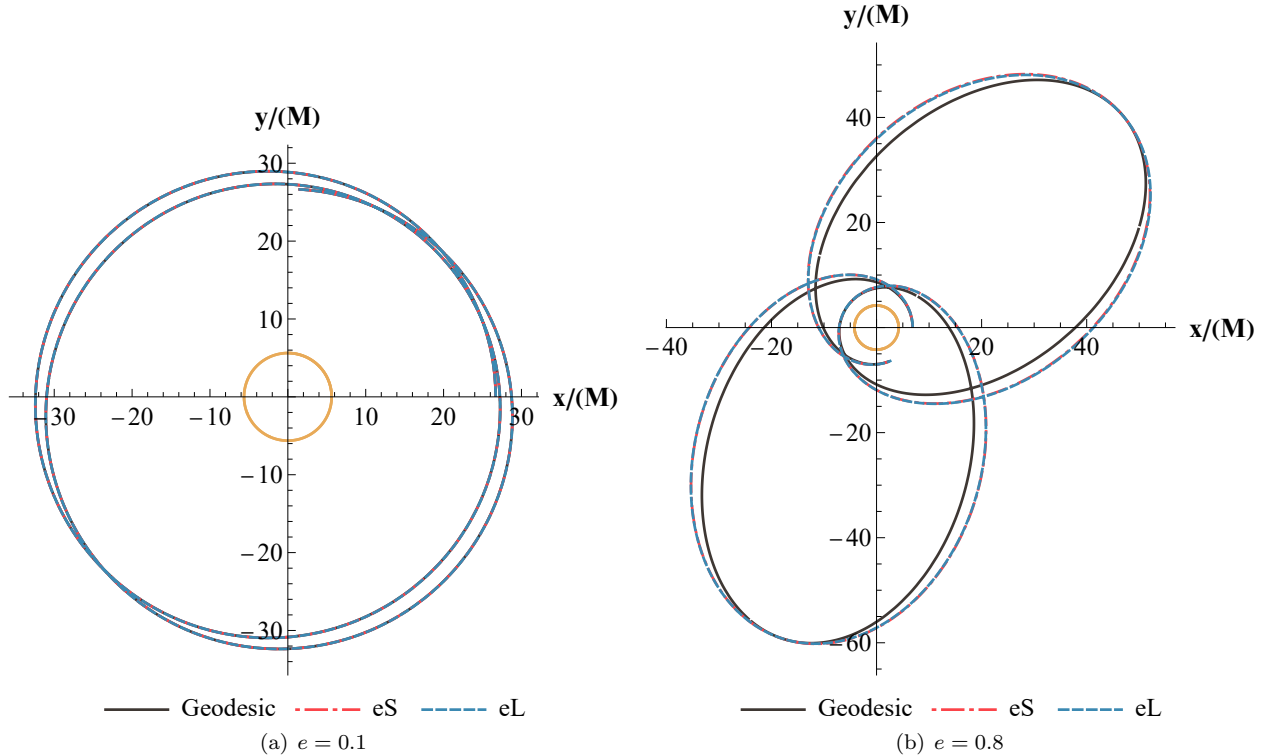


FIG. 1. Equatorial orbits: the solid black line represents high precision numerical result for Eqs. (16)-(19), while the dotted lines with different colors represent the approximate orbits obtained using eL and eS method. The mass of supermassive black hole is set to be $M = 10^6 M_\odot$, and the loop quantum parameter is chosen as $P = 1/1000$. The frequency of ϕ is $\Omega_\phi/(2\pi) = 0.2\text{mHz}$, corresponding to an approximate orbital frequency of $\Omega_r/(2\pi) = 0.14331\text{mHz}$. The small yellow circle at the center represents the minimum periastron of the innermost stable orbit, which is $r_{\text{ISO}} = p_{\text{ISO}}/(1 + e)$.

In Figure 1, we can see that the three methods for obtaining the orbit essentially overlap. The equations (44)-(46) or equations (51) -(53) provide an approximate orbit, which accumulates errors over time. The approximation methods used in equations (55) and (58) introduce periodic errors between the actual orbit and the numerically solved geodesic orbit.

By comparing the obtained orbit with the numerically solved orbit, we can determine that the approximate equations (44)-(46) or equations (51) -(53) we used are reliable. For further error analysis, please refer to Appendix A 2.

B. Adiabatic evolution of frequency and eccentricity

We adopt the following approximation for the Keplerian orbital frequency ν .

$$p = \left(\frac{1 - P}{1 + P} \right)^{2/3} \frac{X}{(2\pi M\nu)^{2/3}}. \quad (59)$$

Combining equations (24), (25), (41), and (42), we can obtain the leading-order equations for the evolution of orbital frequency ν and eccentricity e .

$$\frac{d\nu}{dt} = \frac{\mu^2}{M^3 m} \frac{(1 - P)^6}{(1 + P)^6} \frac{(2\pi M\nu)^{11/3}}{(1 - e^2)^{7/2}} \frac{1}{10\pi} (96 + 292e^2 + 37e^4) + \mathcal{O}((2\pi M\nu)^{13/3}), \quad (60)$$

$$\frac{de}{dt} = -\frac{\mu^2}{15mM^2} \frac{(1 - P)^5}{(1 + P)^6} \frac{(2\pi M\nu)^{8/3}}{(1 - e^2)^{5/2}} \frac{1}{e} (304e^2 + 121e^4 - (192 + 280e^2 - 47e^4)P) + \mathcal{O}((2\pi M\nu)^{10/3}). \quad (61)$$

It should be noted that, as $e \rightarrow 0$, $\Omega_\phi = 2\pi\nu_\phi \rightarrow 2\pi\nu$, which means $\nu \approx \nu_\phi$. Similarly, as $e \rightarrow 1$, $\Omega_r = 2\pi\nu_r \rightarrow 2\pi\nu$, which means $\nu \approx \nu_r$. The detailed analysis can be found in Appendix A 1.

If P is a small quantity less than or equals to $(2\pi M\nu)^{2/3}$, then the leading order correction for P is equal to or less than $3.5PN$, the evolution of ν and e become:

$$\begin{aligned} \frac{d\nu}{dt} &= \frac{\mu^2}{M^3 m} \frac{(1-P)^6}{(1+P)^6} \frac{(2\pi M\nu)^{11/3}}{(1-e^2)^{7/2}} \frac{1}{10\pi} (96 + 292e^2 + 37e^4) \\ &\quad + \frac{96m}{10\pi M^3} \frac{(2\pi M\nu)^{13/3}}{(1-e^2)^{9/2}} \left(\frac{1273}{336} - \frac{2561}{224}e^2 - \frac{3885}{128}e^4 - \frac{13147}{5376}e^6 \right) + \mathcal{O}((2\pi M\nu)^5), \end{aligned} \quad (62)$$

$$\begin{aligned} \frac{de}{dt} &= -\frac{\mu^2}{15mM^2} \frac{(1-P)^5}{(1+P)^6} \frac{(2\pi M\nu)^{8/3}}{(1-e^2)^{5/2}} e \left(304 + 121e^2 - (192 + 280e^2 - 47e^4) \frac{P}{e^2} \right) \\ &\quad - \frac{m}{15M^2} \frac{(2\pi M\nu)^{10/3}}{(1-e^2)^{7/2}} e \left(\frac{1}{56} (70648 - 231960e^2 - 106523e^4) \right) + \mathcal{O}((2\pi M\nu)^4). \end{aligned} \quad (63)$$

Through Eq. (63), we can see that the leading order effect of the P is positive. This means that the correction of LQG tends to increase the orbital eccentricity. As the eccentricity decreases, this effect becomes more significant. Moreover, when the eccentricity approaches

$$e_B = 2\sqrt{\frac{-38 + 35P + \sqrt{1444 - 1208P + 1789P^2}}{121 + 47P}}, \quad (64)$$

the leading-order effect of P will reach the same order as that in the Schwarzschild case. At this point, for the evolution Eq. (63), the precision will degrade to the $2.5PN$ order.

C. Waveforms

In this paper, based on equations (55) and (58), we use the quadrupole waveform [33, 40] as follows:

$$h^{jk} = \frac{2}{r} \ddot{Q}^{jk}. \quad (65)$$

In the previous section, we assumed that the orbit is located in the equatorial plane, which means that the orbital angular momentum direction is $(\theta_L = 0, \phi_L = 0)$. Combining equations (38), (8), (11), and performing a Taylor series expansion, the leading-order gravitational waveform can be expressed as:

$$\begin{aligned} h^{11} &= \mathcal{A}_h \left(2e^2 + 2e \cos(\psi(t)) - 5e \cos(\psi(t) - 2\phi(t)) \right. \\ &\quad \left. - 2e^2 \cos(2\psi(t) - 2\phi(t)) - 4 \cos(2\phi(t)) - e \cos(\psi(t) + 2\phi(t)) \right), \end{aligned} \quad (66)$$

$$\begin{aligned} h^{22} &= \mathcal{A}_h \left(2e^2 + 2e \cos(\psi(t)) + 5e \cos(\psi(t) - 2\phi(t)) \right. \\ &\quad \left. + 2e^2 \cos(2\psi(t) - 2\phi(t)) + 4 \cos(2\phi(t)) + e \cos(\psi(t) + 2\phi(t)) \right), \end{aligned} \quad (67)$$

$$\begin{aligned} h^{12} &= \mathcal{A}_h \left(5e \sin(\psi(t) - 2\phi(t)) + 2e^2 \sin(2\psi(t) - 2\phi(t)) \right. \\ &\quad \left. - 4 \sin(2\phi(t)) - e \sin(\psi(t) + 2\phi(t)) \right), \end{aligned} \quad (68)$$

$$h^{13} = h^{23} = h^{33} = 0, \quad (69)$$

where, $\mathcal{A}_h = m(1-P)^2/(2p(1+P)^2)$. In the actual calculation, we computed up to the second order with p . The traceless gauge of the waveform is given by[33, 40]:

$$h_{\text{TT}}^{jk} = \frac{1}{2} \begin{pmatrix} 0 & 0 & 0 \\ 0 & h^{\theta_s\theta_s} - h^{\phi_s\phi_s} & 2h^{\theta_s\phi_s} \\ 0 & 2h^{\theta_s\phi_s} & h^{\phi_s\phi_s} - h^{\theta_s\theta_s} \end{pmatrix}, \quad (70)$$

where

$$h^{\theta_S \theta_S} = \cos^2 \theta_S (h^{11} \cos^2 \phi_S + h^{12} \sin 2\phi_S + h^{22} \sin^2 \phi_S), \quad (71)$$

$$h^{\theta_S \phi_S} = \cos \theta_S \left(-\frac{1}{2} h^{11} \sin 2\phi_S + h^{12} \cos 2\phi_S + \frac{1}{2} h^{22} \sin 2\phi_S \right), \quad (72)$$

$$h^{\phi_S \phi_S} = h^{11} \sin^2 \phi_S - h^{12} \sin 2\phi_S + h^{22} \cos^2 \phi_S. \quad (73)$$

The polarized gravitational waveforms correspond to: $h_+(t) = h^{\theta_S \theta_S} - h^{\phi_S \phi_S}$ and $h_\times(t) = 2h^{\theta_S \phi_S}$.

IV. RESULTS OF WAVEFORMS

A. Waveforms under eS method

In calculations, we primarily used the ordinary differential equations (ODEs) given by Eqs. (51)-(53) up to (11, 6) orders together with (62) and (63).

As shown in Fig. 2, by numerically solving equations (62) and (63), we can obtain the evolution of eccentricity e and frequency ν_ϕ with time. In the figure, the red dot represents the orbit reaching ISO, where the ISO is calculated in Appendix B. It can be observed that with increasing P , both the decay rate of e and the growth rate of ν_ϕ decrease. Additionally, as shown in Fig. 2(a), when eccentricity e is smaller than the limit e_B in Eq. (64), the leading order term in Eq. (63) becomes positive. When the leading order dominates, the eccentricity gradually increases during evolution. It is important to note that when the eccentricity evolves close to or below the dashed line, the accuracy of eccentricity evolution changes from $3.5PN$ to $2.5PN$. On the other hand, with increasing P , The growth rate of ν_ϕ slows down. This implies that the quantum effect of the inspiraling binary plays a role similar to repulsion (reducing the impact of massive black holes).

Fig. 3(a) shows the evolution of accumulated phase difference $\Delta\Phi = \Phi(P) - \Phi(P=0)$ with time for various values of initial eccentricities e_0 and P . It can be seen that with $e_0 = 0.1$, as P increases, $\Delta\Phi$ increases faster. When $P = 1/1000$, $\Delta\Phi$ grows more rapidly with increasing eccentricity, although the change is not significant.

After performing the above calculations, we obtained the corresponding evolutions of $(\Psi, \nu_\phi, e_0, \gamma)$. Combining this with quadrupole waveform, we can obtain the gravitational waveforms for different values of e_0 and P , as shown in Fig. 4.

In Fig. 4, it can be observed that when $e_0 = 0.1$ and $P = 1/10000$, it takes around 100 days for the gravitational waveforms to show a significant difference. On the other hand, when $P = 1/1000$, the difference becomes apparent in just 30 days. This is consistent with the conclusions in Fig. 3(a). Similarly, when P is fixed, the variation in eccentricity does not have a significant impact at which the gravitational waveforms exhibit noticeable phase differences. Moreover, each vertical line in the Fig. 4 represents the time interval $T_\phi = 1/\nu_\phi(t=0)$. We can find the GW frequency $\nu_{GW}(t=0) \approx 2\nu_\phi(t=0)$, which is consistent with Ref. [34].

B. Waveforms under eL method

The gravitational waveforms obtained through the large eccentricity method, described by equations (44)-(46) up to (10, 5) orders with (62) and (63), can be used to generate waveforms for different values of e and P . Waveforms are illustrated in Fig. 5. It can be observed that when e_0 is fixed, a larger P leads to a shorter time for significant differences to appear in the gravitational waveforms. Similarly, when P is fixed, a larger e_0 results in a shorter time for noticeable differences in the waveforms. This trend is consistent with the evolution of $\Delta\Phi$ observed at smaller eccentricities.

V. PARAMETER ESTIMATION

For a three arm spacebased GW detector, different sets of Michelson interferometers can be constructed by choosing different optical paths. The strain amplitude of the detector can be described by the unified expression:

$$h(t) = \frac{1}{D} \frac{\sqrt{3}}{2} (F^+(t)h_+(t) + F^\times(t)h_\times(t)), \quad (74)$$

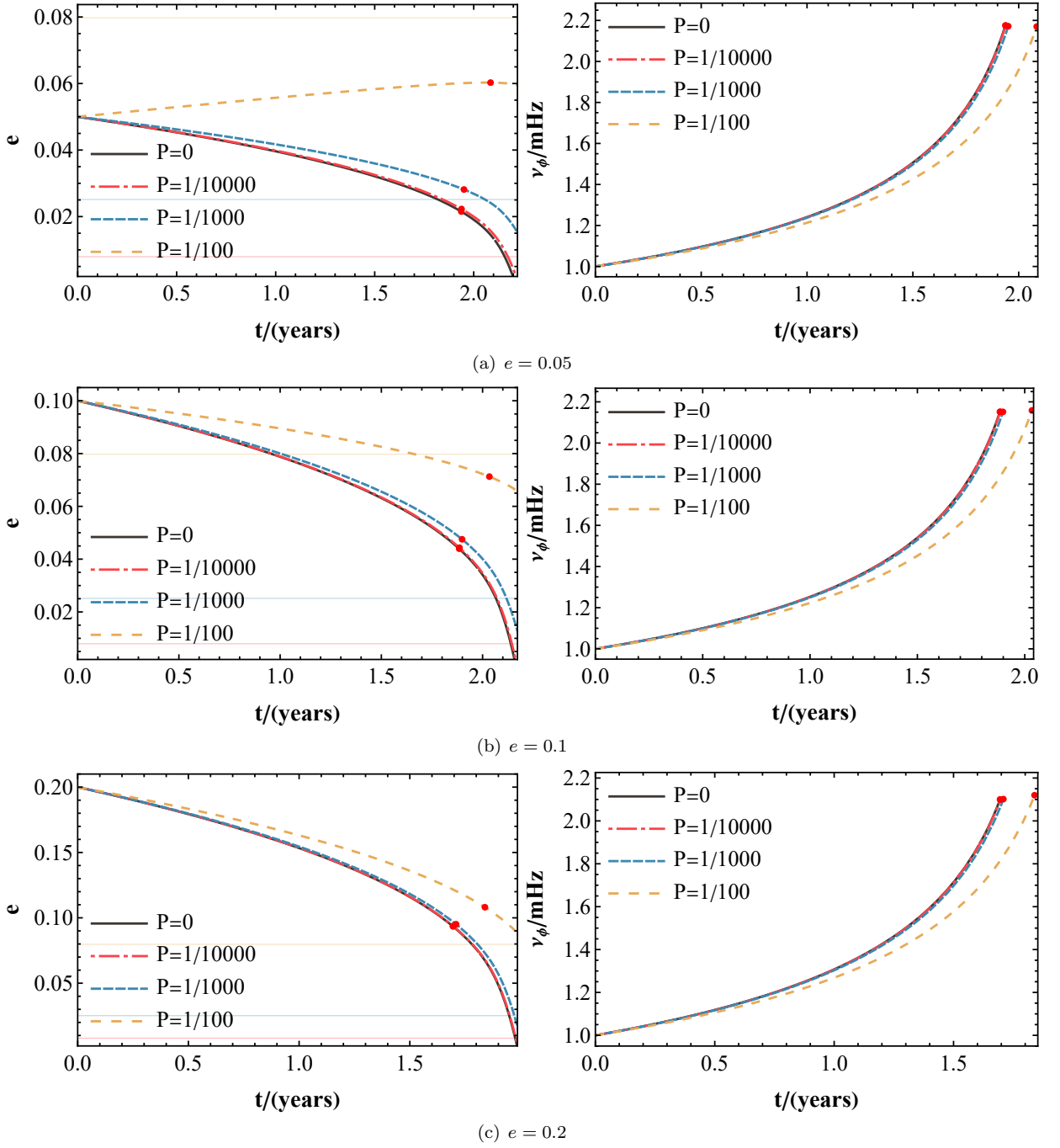


FIG. 2. The evolution of e and ν_ϕ for different initial eccentricities ($e_0 = 0.2, 0.1, 0.05$) and an initial frequency of $\nu_\phi = 1\text{mHz}$. The different horizontal lines in the background represent the critical eccentricity e_B . The red dot indicates the position of ISO.

where the distance D represents the separation between the observer and the GW source, while $F^+(t)$ and $F^\times(t)$ denote the antenna functions. These functions depend on both the direction of the source (θ_S, ϕ_S) and the orbital angular momentum direction ($\theta_L = 0, \phi_L = 0$). The specific mathematical expressions can be found in references [32, 41], where it is stated that these antenna functions have a period of one year ($T_{ap} = 1\text{year}$), with initial parameter angles set to $\bar{\alpha}_0 = \bar{\phi}_0 = 0$. Therefore, the GW signal is completely determined by the parameters $\lambda = (M, m = 10M_\odot, P, \Phi_0 \approx 0, e_0, \nu_0(\text{or } t_0), \hat{\gamma}_0 = 0, \theta_S = \pi/2, \phi_S = \pi/2, \theta_L = 0, \phi_L = 0, D = 1\text{Gpc})$ where e_0 is the initial eccentricity of the orbit, and ν_0 is the initial frequency of the orbit, corresponding to the chosen time range of the data. For example, in our data sampling, we select the data within $t_0 = 1\text{year}$ before the plunge $p_{\text{plunge}} = p + \delta p$,

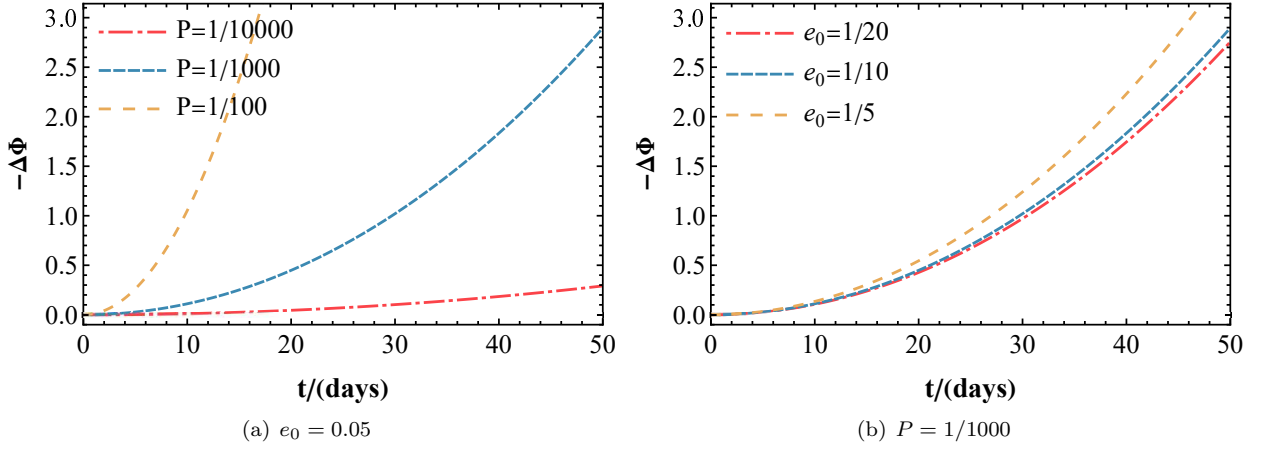


FIG. 3. The accumulated orbital phase difference $\Delta\Phi = \Phi(P) - \Phi(P = 0)$ under different values of P or e_0 with $M = 10^6 M_\odot$ and $m = 10M_\odot$.

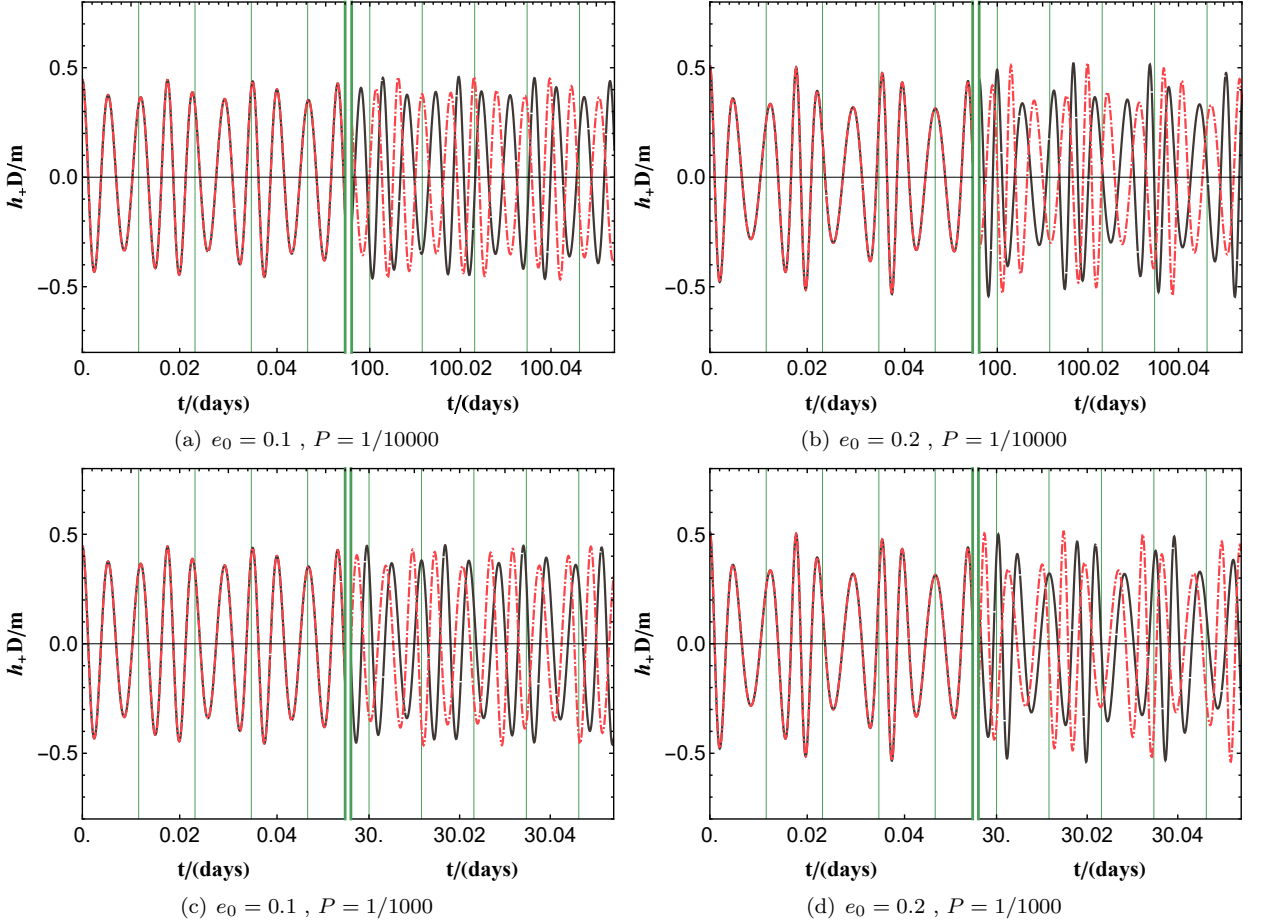


FIG. 4. The gravitational waveforms under $e_0 = \{1/10, 1/5\}$ and $P = \{1/10000, 1/1000\}$. The solid black line represents the waveform with $P = 0$. The left side of each plot shows the initial waveforms, while the right side shows the ones after a period of evolution.

where a fixed shift $\delta p = 0.1$ is applied. The corresponding ν_0 will be obtained. For the chosen source azimuthal angles ($\theta_S = \pi/2, \phi_S = \pi/2$), this implies that $h_+ = h^{11}$ and $h_\times = 0$. In the subsequent calculations, we mainly consider the varying parameters (M, P, e_0), while the remaining parameters are set to the aforementioned values.

To assess the effects of the varying parameters, the noise weighted inner product between two templates need to be

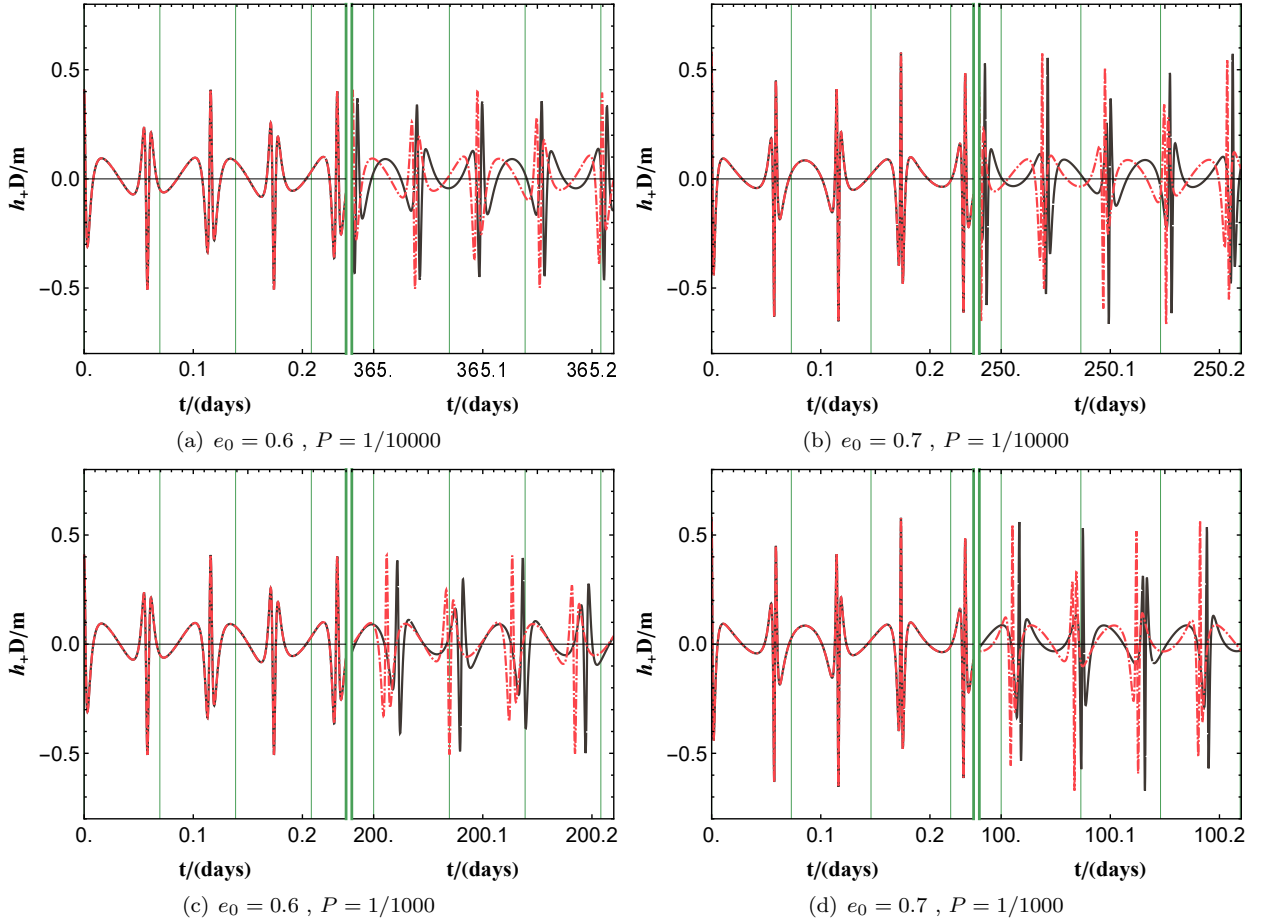


FIG. 5. The gravitational waveforms under different eccentricities $e_0 = \{0.6, 0.7\}$ and different loop quantum parameters $P = \{1/10000, 1/1000\}$. The left side of each plot represents the initial waveforms, while the right side displays the ones after a period of evolution.

introduce as [42, 43]:

$$\langle h_e | h_m \rangle = 2 \int_0^\infty \frac{h_e^*(f)h_m(f) + h_e(f)h_m^*(f)}{S_n(f)} df, \quad (75)$$

where $h_e(f)$ and $h_m(f)$ are the frequency domain results of the $h_e(t)$ and $h_m(t)$ after Discrete Fourier transformation(DFT), respectively. $*$ denotes complex conjugation. $S_n(f)$ is the noise power spectral density(PSD) of the space-borne GW detector, such as LISA [27, 44]. Note that a Tukey window function with a cosine fraction of 0.01 is used before DFT and the sampling frequencies of the GW signals are analyzed in Appendix C.

ρ represents the signal-to-noise ratio (SNR) of a signal, given by $\rho = \sqrt{\langle h | h \rangle}$. We can define faithfulness as:

$$\mathcal{F}[P_e, P_m] = \frac{\langle h_{P=P_e} | h_{P=P_m} \rangle}{\sqrt{\langle h_{P=P_e} | h_{P=P_e} \rangle \langle h_{P=P_m} | h_{P=P_m} \rangle}}. \quad (76)$$

The corresponding mismatch is defined as:

$$\mathcal{O}[P_e, P_m] = 1 - \mathcal{F}[P_e, P_m]. \quad (77)$$

When the mismatch \mathcal{O} is larger than $\sim \mathcal{D}/(2\rho^2)$ (\mathcal{D} represents the parameter space of the model, which is approximately 10), it indicates significant differences between two GW signals and they cannot faithfully describe each other. For a signal with an SNR of 30, this requires a mismatch $\mathcal{O} \gtrsim 0.012$ ($\log_{10} \mathcal{O} \lesssim -1.92$) [42, 43].

Fig. 6 shows the constraint capability of the LISA detector on P for eccentricities $e_0 = 0.05, 0.1$ and different central black hole masses. From these figures, it can be seen that for one year of GW detection, the constraint capability of

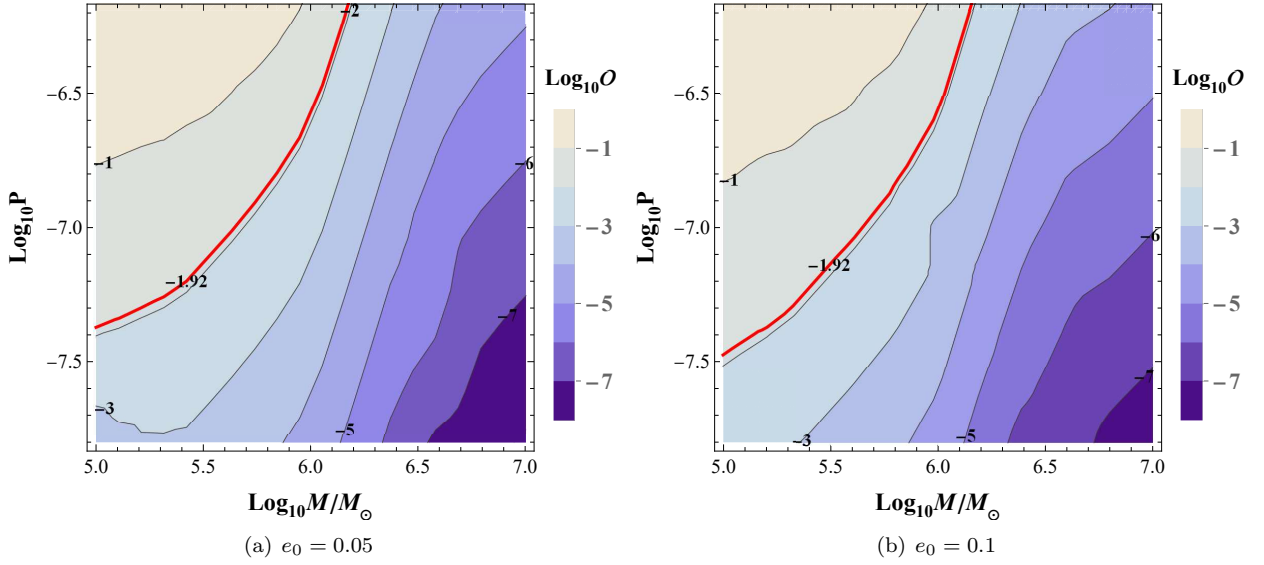


FIG. 6. Mismatch of LISA under different values of M and P . The red line represents a boundary where mismatch $\mathcal{O} = 0.012$ ($\log_{10} \mathcal{O} = -1.92$).

LISA on P increases as the mass decreases within the range of $M = 1 \times 10^5 M_\odot \sim 1 \times 10^7 M_\odot$. This is because as M decreases from $1 \times 10^7 M_\odot$ to $1 \times 10^5 M_\odot$, the frequency ν_ϕ around ISO goes from about $\sim 0.2\text{mHz}$ to $\sim 20\text{mHz}$, which is close to the LISA detector's most sensitive frequency $\sim 10\text{mHz}$. At the same time, the energy and angular momentum flux(fluxes?) increase as M decreases.

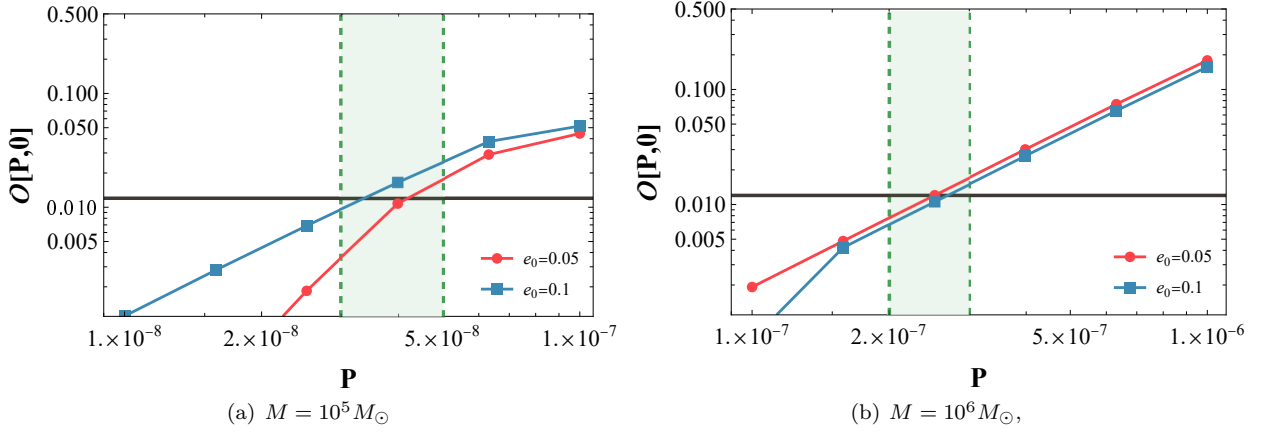


FIG. 7. Mismatch as a function of P with different values of e for LISA. The Black line represents a boundary where mismatch $\mathcal{O} = 0.012$

Fig. 7 presents mismatch as a function of P with different values of e for LISA, in more detail. From Fig. 7(a), it can be seen that for one year of GW detection with $M = 1 \times 10^5 M_\odot$, LISA achieves a constraint capability of $3 \times 10^{-8} \sim 5 \times 10^{-8}$. When $M = 1 \times 10^6 M_\odot$, as shown in Figure 7(b), LISA achieves a constraint capability of $2 \times 10^{-7} \sim 3 \times 10^{-7}$.

VI. CONCLUSION

In this paper, we consider the modified AK waveform in the EMRI system under the background of self-dual spacetime in loop quantum gravity. First, we calculate the motion equations of the test body in a self-dual spacetime and obtain the two orbital frequencies on the equatorial plane in the weak field limit. Then, combining the energy and angular momentum flux carried by the gravitational waves under the quadrupole moment approximation, we obtain

the adiabatic orbit of the test body. Using different fundamental frequencies ν_r or ν_ϕ , we get two methods applied to different values of e .

Through numerical calculations, we found that slight perturbations of P will be amplified after one year of orbit evolution, and the final waveform results are significantly different from those without the perturbation of P . Among them, the smaller the mass M of the central black hole, the stronger the constraint ability of LISA on the loop quantum parameters, in the range of $M \in [1 \times 10^5 M_\odot, 1 \times 10^7 M_\odot]$. Specially, the ability to constrain P will be approached the upper limit of about $3 \times 10^{-8} \sim 5 \times 10^{-8}$ with $M = 1 \times 10^5 M_\odot$ for small changes in e near zero. Overall, compared with the best constraint from the Cassini experiment in the solar system, $P \leq 5.5 \times 10^{-6}$ [24], the constraint capability will be improved by 1 to 2 orders of magnitude.

We only consider the self-dual spacetime in this paper, however, the methods described in the current paper can also be generalised to other loop quantum black hole models [7, 12, 14, 45, 46] and obtain the constraint on the relevant quantum parameter. We would like to leave these interesting topics for future study.

ACKNOWLEDGMENTS

This work is supported by National Natural Science Foundation of China with No. 12275087.

Appendix A: Error analysis

1. Error of Frequency

Note that when $P = 0$, equations (29) and (30) reduce to the Schwarzschild case. We obtain:

$$\begin{aligned} \Omega_\phi &= \frac{X^{3/2}}{Mp^{3/2}} + \left(\frac{3X^{3/2}}{M} - \frac{3X^{5/2}}{M} \right) \frac{1}{p^{5/2}} + \left(\frac{57X^{3/2}}{4M} - \frac{63X^{5/2}}{4M} - \frac{15X^3}{2M} + \frac{9X^{7/2}}{M} \right) \frac{1}{p^{7/2}} \\ &+ \left(\frac{315X^{3/2}}{4M} - \frac{96X^{5/2}}{M} - \frac{60X^3}{M} + \frac{237X^{7/2}}{4M} + \frac{45X^4}{M} - \frac{27X^{9/2}}{M} \right) \frac{1}{p^{9/2}} + \mathcal{O}\left(\frac{1}{p^{11/2}}\right), \end{aligned} \quad (\text{A1})$$

$$\begin{aligned} \Omega_r &= \frac{X^{3/2}}{Mp^{3/2}} - \frac{3X^{5/2}}{Mp^{5/2}} + \left(-\frac{6X^{5/2}}{M} - \frac{15X^3}{2M} + \frac{9X^{7/2}}{M} \right) \frac{1}{p^{7/2}} \\ &+ \left(-\frac{24X^{5/2}}{M} - \frac{75X^3}{2M} + \frac{30X^{7/2}}{M} + \frac{45X^4}{M} - \frac{27X^{9/2}}{M} \right) \frac{1}{p^{9/2}} + \mathcal{O}\left(\frac{1}{p^{11/2}}\right). \end{aligned} \quad (\text{A2})$$

Interestingly, even if we calculate Ω_ϕ and Ω_r up to $\mathcal{O}(p^{-23/2})$, we can still obtain the following approximation:

$$\Omega_\phi \rightarrow \frac{X^{3/2}}{Mp^{3/2}}, \quad \text{When } e \rightarrow 0 (X \rightarrow 1); \quad (\text{A3})$$

$$\Omega_r \rightarrow \frac{X^{3/2}}{Mp^{3/2}}, \quad \text{When } e \rightarrow 1 (X \rightarrow 0). \quad (\text{A4})$$

From the Fig. 8, we can see that when $e \rightarrow 0$, assuming $\Omega_\phi = 2\pi\nu_\phi \approx \nu = X^{3/2}/Mp^{3/2}$ can achieve better accuracy. When the parameter P is small, it is only a small correction to the Eqs. (A1)-(A2), as shown below:

$$\Omega_\phi \rightarrow \frac{(1-P)X^{3/2}}{(1+P)Mp^{3/2}} + \mathcal{O}(P), \quad \text{When } e \rightarrow 0 (X \rightarrow 1); \quad (\text{A5})$$

$$\Omega_r \rightarrow \frac{(1-P)X^{3/2}}{(1+P)Mp^{3/2}} + \mathcal{O}(P), \quad \text{When } e \rightarrow 1 (X \rightarrow 0). \quad (\text{A6})$$

Therefore, we can assume the leading order to be

$$\Omega_\phi = 2\pi\nu_\phi \rightarrow 2\pi\nu, \quad \text{When } e \rightarrow 0 (X \rightarrow 1); \quad (\text{A7})$$

$$\Omega_r = 2\pi\nu_r \rightarrow 2\pi\nu, \quad \text{When } e \rightarrow 1 (X \rightarrow 0). \quad (\text{A8})$$

In addition, when $e \rightarrow 0$, $\nu_r(p)$ is not a monotonic function outside the ISO, causing problems with the series

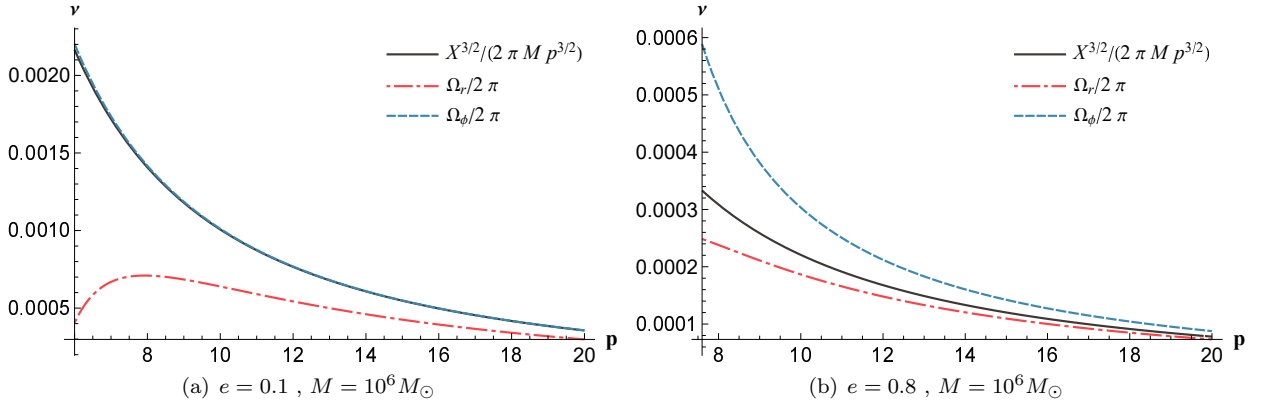


FIG. 8. Relationship between the Kepler frequency $\nu = X^{3/2}/M p^{3/2}$, the anomaly frequency $\Omega_r/(2\pi)$ and the “longitude” frequency $\Omega_\phi/(2\pi)$ with respect to p . Among them, Ω_r and Ω_ϕ are both accurate to $\mathcal{O}(p^{-21/2})$ order.

expansion of its inverse function $p(\nu_r)$, which is a multivalued one. When $e \rightarrow 1$, the inverse series expansion $p(\nu_\phi)$ in Eq. (49) of $\nu_\phi(p)$ converges very slowly near the ISO.

In summary, we have $\nu_\phi \approx \nu$ when $e \rightarrow 0$ and $\nu_r \approx \nu$ while $e \rightarrow 1$.

2. Error of Geodesic orbit

In the AK equation, when the energy flux and angular momentum flux tend to zero, the accumulated error of geodesic orbit is mostly concentrated in the accumulated error of $\hat{\gamma}$. Therefore, the error of the orbital approximation can be determined by Eqs. (44)-(46) or Eqs. (51)-(53) together with Eqs. (16)-(19).

Now, let us consider the case when

$$\{e = 0.1(\text{or } 0.8), \nu_\phi = 0.2 \text{ mHz}, M = 10^6 M_\odot, P = 1/1000\}$$

Thus, $\hat{\gamma}$ can be expanded in a series using $(2\pi M \nu_\phi)^{2/3}$ (or $(2\pi M \nu_r)^{2/3}$), and the effects of different orders in the expansion are shown in Fig. 9 and 10:

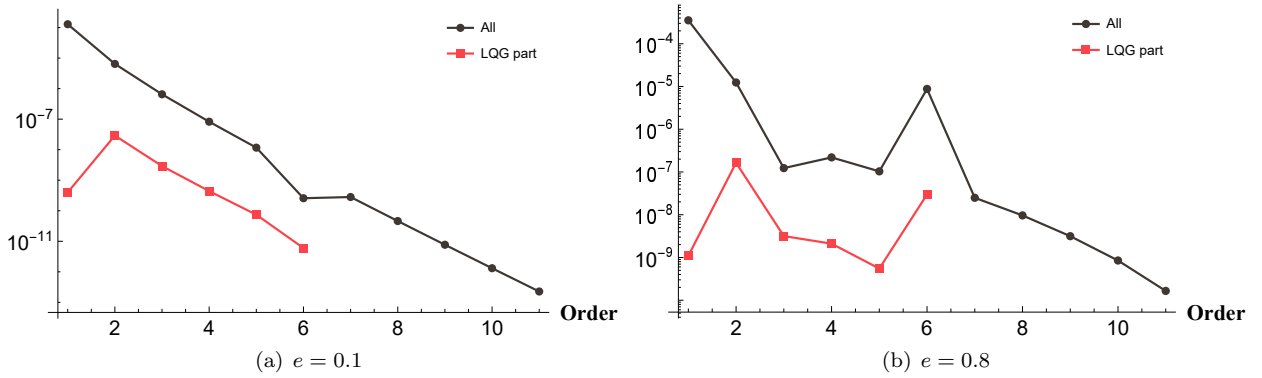


FIG. 9. Influence of different order under eS method.

The black dotted line represents the magnitude of each order in the series expansion of $\hat{\gamma}$. The red square dotted line represents the magnitude of each order caused by the LQG effect. It can be seen that both methods achieve high accuracy. The convergence rate of the eS method is faster overall, while the eL one is more stable.

In Fig. 11, the difference between the precessional angle, $\gamma(t) = \phi(t) - \psi(t)$, obtained by numerically solving Eqs. (16)-(19) and the approximate one in the AK method, $\gamma_{Ap} = \phi_{Ap} - \psi_{Ap}$ (see equations 55 and 58), is shown as $\delta\hat{\gamma}$.

It can be seen from Fig. 11(a) that when $e \rightarrow 0$ such as $e = 0.1$, after one year of evolution, the value of $\delta\hat{\gamma}$ is still much smaller than 1 rad, and the eS method is better than the eL one. when $e \rightarrow 1$ such as $e = 0.8$, the $\delta\hat{\gamma}$ from eL method increases rapidly, which is due to the slow convergence as shown in Fig. 10(b). For example, the

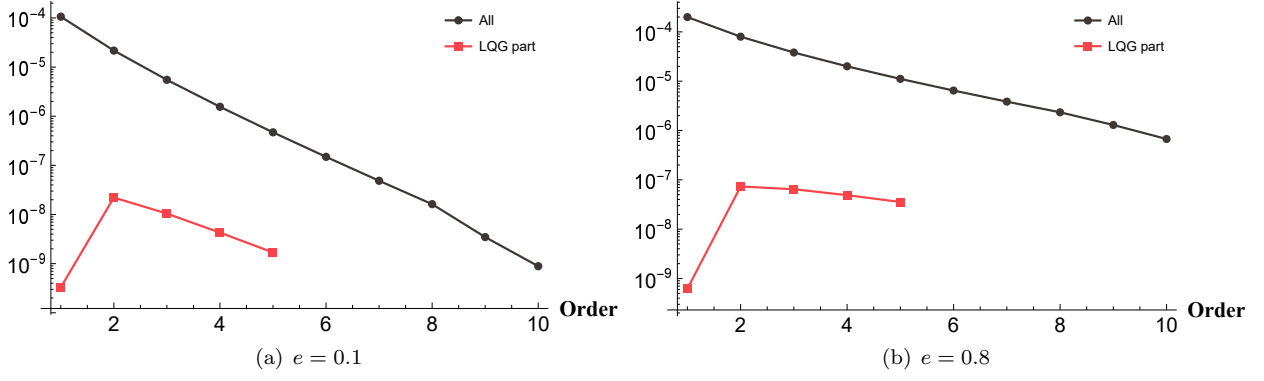
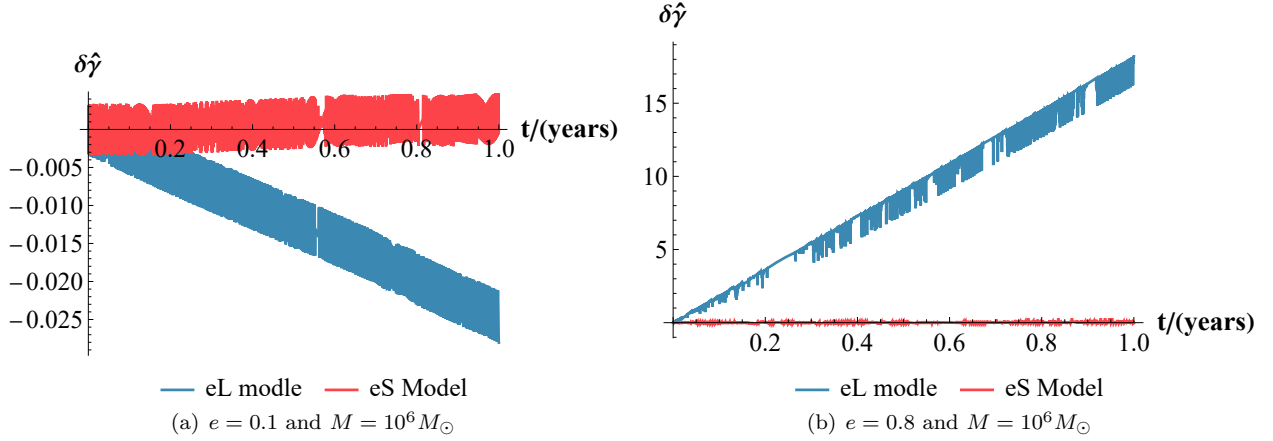


FIG. 10. Influence of different order under eL method.

FIG. 11. Error of $\hat{\gamma}$ for 1 year.

accuracy at the 10th order is approximately 5×10^{-7} , which means that the error $\delta\hat{\gamma}$ after one year is approximately $5 \times 10^{-7}(\text{year/s}) \text{ rad} = 15\text{rad}$, consistent with Fig. 11(b). This further confirms the previous conclusion. Note that the error is not a line but is caused by the periodic error of γ_{Ap} . In conclusion, when the initial eccentricity e is relatively small, we apply the eS method, using ν_ϕ as the fundamental frequency, for the calculation and analysis of gravitational waveforms.

Appendix B: Innermost stable orbit

Note that a_0 appears in the higher order terms and is a very small quantity that can be set to zero. To find the ISO, we can make $d((dr/d\tau)^2)/dr = 0$ at the pericenter r_{peri} [47, 48]. Combining equations (9), (20), and (21), we obtain the separatrix equation

$$\begin{aligned}
0 = & 512e(1+e)^3(3+e(-2+3e))P^7 - 32e(1+e)^2P^5(1+P)^2\mathcal{S}_1p \\
& + 16e(1+e)P^3(1+P)^4\mathcal{S}_2p^2 + 8e(1+e)P^2(1+P)^6\mathcal{S}_3p^3 \\
& + 4e(1+e)(-1+P)^2P(1+P)^8(15+8e+e^2-2(5+e(2+e))P+(3+e)(5+e)P^2)p^4 \\
& + 2e(1+e)(-1+P)^2(1+P)^{10}(3+e-(5+e)P+(3+e)P^2)p^5 \\
& - e(1+e)(-1+P)^2(1+P)^{12}p^6,
\end{aligned} \tag{B1}$$

where

$$\mathcal{S}_1 = 37 + 8e^3(-1 + P)^2 + e^4(-1 + P)^2 - 16eP + P(-50 + 37P) + 6e^2(3 + P(-2 + 3P)), \quad (\text{B2})$$

$$\begin{aligned} \mathcal{S}_2 = & 15 + e^4(-1 + P)^2(1 + (-1 + P)P) \\ & + 2e^3(-1 + P)^2(3 + P(-2 + 3P)) - 6e^2P(5 + P(-6 + 5P)) \\ & + P(-71 + P(88 + P(-71 + 15P))) + 2e\left(5 + P(-36 + P(38 + P(-36 + 5P)))\right), \end{aligned} \quad (\text{B3})$$

$$\begin{aligned} \mathcal{S}_3 = & 27 + e^3(-1 + P)^4 + e^2(-1 + P)^2(1 + (-14 + P)P) + P(-64 + P(98 + P(-64 + 27P))) \\ & + e\left(19 + P(-44 + P(74 + P(-44 + 19P)))\right), \end{aligned} \quad (\text{B4})$$

Assuming P is small and accurate up to second order of P , the approximate solution to the equation is obtained as

$$p = 6 + 2e - (12 + 4e)P + \frac{6(35 + 35e + 9e^2 + e^3)}{(3 + e)^2}P^2. \quad (\text{B5})$$

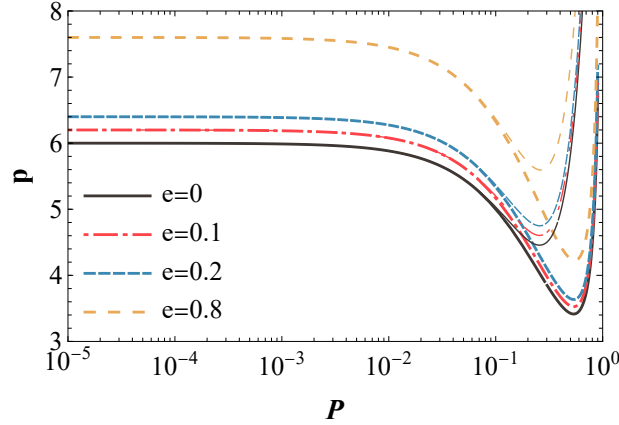


FIG. 12. For different values of e , the p of ISO respect to P , where the thick line is the numerical solution of Eq. (B1), while the thin lines are the approximate solutions of Eq. (B5).

From the Fig. 12, when P is less than 0.01, the approximate solution can be obtained with high precision. For example, when the parameters are $\{P = 1/100, e = 0.2\}$, we take the approximate $p = 6.27448$, and the corresponding numerical solution to Eq. (B1) is $p = 6.27445$, with a relative error of approximately 5.8×10^{-6} .

Appendix C: Discrete Fourier transform

Fig. 13 shows $h(f)$ from DFT of $h(t)$. It can be seen that as the eccentricity decreases, the contribution of the GW frequency $\nu = 2\nu_\phi + \mathbf{n}\nu_r$, $\mathbf{n} = \pm 1, \pm 2, \dots$ becomes more and more significant. In particular, the contribution of $\nu = 2\nu_\phi$ reaches its maximum value. This is consistent with the fact that as $e \rightarrow 0$, the GW frequency approaches $2\nu_\phi$. Moreover, for $e = 0.1$, the contributions of frequencies $\nu = 2\nu_\phi + 2\nu_r$ cannot be neglected. When the signal is sampled, the sampling frequency can be selected as $f_{Ny} = 2\nu_\phi + 2\nu_r < 4\nu_\phi$.

For example, in the case of $M = 10^6 M_\odot$, with an initial eccentricity of $e = 0.2$, after 1 year of evolution to the innermost stable orbit, the eccentricity is still approximately $e \approx 0.1$ and corresponds to $\nu_\phi \approx 2\text{mHz}$ and $\nu_r \approx 0.5\text{mHz}$. At this point, the sampling frequency $f_S = 2.5(2\nu_\phi + 2\nu_r) \approx 12.5\text{mHz}$.

[1] C. Rovelli, Quantum Gravity, Cambridge University Press, 2004.

[2] T. Thiemann, Modern Canonical Quantum General Relativity, Cambridge University Press, 2007.

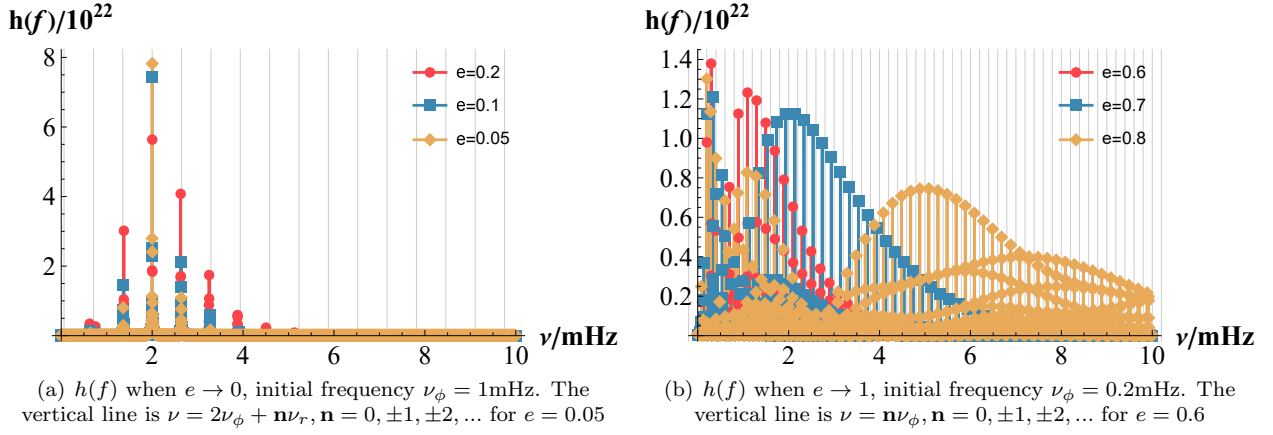


FIG. 13. $h(f)$ from DFT of $h(t)$ for $e = 0.05, 0.1, 0.2$ with $P = 0.001$.

- [3] A. Ashtekar and J. Lewandowski, Background independent quantum gravity: A status report, *Class. Quant. Grav.* 21, R53 (2004).
- [4] M. Han, W. Huang, and Y. Ma, Fundamental structure of loop quantum gravity, *Int. J. Mod. Phys. D* 16, 1397 (2007).
- [5] M. Bojowald, Absence of a Singularity in Loop Quantum Cosmology, *Phys. Rev. Lett.* 86, 5227 (2001).
- [6] L. Modesto, Disappearance of the Black Hole Singularity in Loop Quantum Gravity, *Phys. Rev. D* 70, 124009 (2004).
- [7] A. Ashtekar and M. Bojowald, Quantum Geometry and the Schwarzschild Singularity, *Class. Quantum Grav.* 23, 391 (2005).
- [8] A. Ashtekar, M. Bojowald, and J. Lewandowski, Mathematical Structure of Loop Quantum Cosmology, *Advances in Theoretical and Mathematical Physics* 7, 233 (2003).
- [9] M. Bojowald, Loop Quantum Cosmology, *Living Rev. Relativ.* 11, 4 (2008).
- [10] A. Ashtekar and P. Singh, Loop Quantum Cosmology: A Status Report, *Class. Quantum Grav.* 28, 213001 (2011).
- [11] C. G. Boehmer and K. Vandersloot, Loop Quantum Dynamics of the Schwarzschild Interior, *Phys. Rev. D* 76, 104030 (2007).
- [12] X. Zhang, Loop Quantum Black Hole, *Universe* 9, 7 (2023).
- [13] L. Modesto, Semiclassical Loop Quantum Black Hole, *Int J Theor Phys* 49, 1649 (2010).
- [14] L. Modesto, Loop Quantum Black Hole, *Class. Quantum Grav.* 23, 5587 (2006).
- [15] L. Modesto, Semiclassical Loop Quantum Black Hole, *Int J Theor Phys* 49, 1649 (2010).
- [16] C. M. Will, The Confrontation between General Relativity and Experiment, *Living Rev. Relativ.* 17, 4 (2014).
- [17] J. H. Taylor, Binary Pulsars and Relativistic Gravity, *Rev. Mod. Phys.* 66, 711 (1994).
- [18] N. Yunes and D. N. Spergel, Double-Binary-Pulsar Test of Chern-Simons Modified Gravity, *Phys. Rev. D* 80, 042004 (2009).
- [19] B. Seymour and K. Yagi, Testing General Relativity with Black Hole-Pulsar Binaries, *Phys. Rev. D* 98, 124007 (2018).
- [20] K. Akiyama, A. Alberdi, et al. (EHT Collaboration), First M87 Event Horizon Telescope Results. I. The Shadow of the Supermassive Black Hole, *Astrophys. J. Lett.* 875, L1 (2019).
- [21] D. Psaltis, L. Medeiros, et al. (EHT Collaboration), Gravitational Test beyond the First Post-Newtonian Order with the Shadow of the M87 Black Hole, *Phys. Rev. Lett.* 125, 141104 (2020).
- [22] B. P. Abbott, R. Abbott, T. D. Abbott, et al. (LIGO Scientific and Virgo Collaborations), Tests of General Relativity with GW150914, *Phys. Rev. Lett.* 116, 221101 (2016).
- [23] S. Sahu, K. Lochan, and D. Narasimha, Gravitational Lensing by Self-Dual Black Holes in Loop Quantum Gravity, *Phys. Rev. D* 91, 063001 (2015).
- [24] T. Zhu and A. Wang, Observational Tests of the Self-Dual Spacetime in Loop Quantum Gravity, *Phys. Rev. D* 102, 124042 (2020).
- [25] J.-M. Yan, Q. Wu, C. Liu, T. Zhu, and A. Wang, Constraints on Self-Dual Black Hole in Loop Quantum Gravity with S0-2 Star in the Galactic Center, *J. Cosmol. Astropart. Phys.* 2022, 008 (2022).
- [26] C. Liu, H. Xu, H. Siew, T. Zhu, Q. Wu, and Y. Zhao, Constraints on the Rotating Self-Dual Black Hole with Quasi-Periodic Oscillations, *arXiv:2305.12323*.
- [27] P. Amaro-Seoane et al., Laser Interferometer Space Antenna, *arXiv:1702.00786*.
- [28] J. Mei et al., The TianQin Project: Current Progress on Science and Technology, *Progress of Theoretical and Experimental Physics* 2021, 05A107 (2021).
- [29] G. Wang, W.-T. Ni, W.-B. Han, P. Xu, and Z. Luo, Alternative LISA-TAIJI Networks, *Phys. Rev. D* 104, 024012 (2021).
- [30] W.-R. Hu and Y.-L. Wu, The Taiji Program in Space for Gravitational Wave Physics and the Nature of Gravity, *National Science Review* 4, 685 (2017).
- [31] S. Babak, J. Gair, A. Sesana, E. Barausse, C. F. Sopuerta, C. P. L. Berry, E. Berti, P. Amaro-Seoane, A. Petiteau, and A. Klein, Science with the Space-Based Interferometer LISA. V. Extreme Mass-Ratio Inspirals, *Phys. Rev. D* 95, 103012 (2017).

- (2017).
- [32] L. Barack and C. Cutler, LISA Capture Sources: Approximate Waveforms, Signal-to-Noise Ratios, and Parameter Estimation Accuracy, *Phys. Rev. D* 69, 082005 (2004).
 - [33] S. Babak, H. Fang, J. R. Gair, K. Glampedakis, and S. A. Hughes, “Kludge” Gravitational Waveforms for a Test-Body Orbiting a Kerr Black Hole, *Phys. Rev. D* 75, 024005 (2007).
 - [34] A. J. K. Chua and J. R. Gair, Improved Analytic Extreme-Mass-Ratio Inspirational Model for Scoping out eLISA Data Analysis, *Class. Quantum Grav.* 32, 232002 (2015).
 - [35] A. J. K. Chua, C. J. Moore, and J. R. Gair, Augmented Kludge Waveforms for Detecting Extreme-Mass-Ratio Inspirals, *Phys. Rev. D* 96, 044005 (2017).
 - [36] M. L. Katz, A. J. K. Chua, L. Speri, N. Warburton, and S. A. Hughes, Fast Extreme-Mass-Ratio-Inspirational Waveforms: New Tools for Millihertz Gravitational-Wave Data Analysis, *Phys. Rev. D* 104, 064047 (2021).
 - [37] L. Speri, M. L. Katz, A. J. K. Chua, S. A. Hughes, N. Warburton, J. E. Thompson, C. E. A. Chapman-Bird, and J. R. Gair, Fast and Fourier: Extreme Mass Ratio Inspirational Waveforms in the Frequency Domain, arXiv:2307.12585.
 - [38] R. Fujita and W. Hikida, Analytical Solutions of Bound Timelike Geodesic Orbits in Kerr Spacetime, *Class. Quantum Grav.* 26, 135002 (2009).
 - [39] K. S. Thorne, Multipole Expansions of Gravitational Radiation, *Rev. Mod. Phys.* 52, 299 (1980).
 - [40] M. Maggiore, *Gravitational Waves: Volume 1: Theory and Experiments* (Oxford University Press, 2007).
 - [41] T. A. Apostolatos, C. Cutler, G. J. Sussman, and K. S. Thorne, Spin-Induced Orbital Precession and Its Modulation of the Gravitational Waveforms from Merging Binaries, *Phys. Rev. D* 49, 6274 (1994).
 - [42] E. E. Flanagan and S. A. Hughes, Measuring Gravitational Waves from Binary Black Hole Coalescences. I. Signal to Noise for Inspirational, Merger, and Ringdown, *Phys. Rev. D* 57, 4535 (1998).
 - [43] L. Lindblom, B. J. Owen, and D. A. Brown, Model Waveform Accuracy Standards for Gravitational Wave Data Analysis, *Phys. Rev. D* 78, 124020 (2008).
 - [44] A. Maselli, N. Franchini, L. Gualtieri, T. P. Sotiriou, S. Barsanti, and P. Pani, Detecting Fundamental Fields with LISA Observations of Gravitational Waves from Extreme Mass-Ratio Inspirals, *Nat Astron* 6, 4 (2022).
 - [45] A. Ashtekar, J. Olmedo, and P. Singh, Quantum Extension of the Kruskal Spacetime, *Phys. Rev. D* 98, 126003 (2018).
 - [46] N. Bodendorfer, F. M. Mele, and J. Münch, Mass and Horizon Dirac Observables in Effective Models of Quantum Black-to-White Hole Transition, *Class. Quantum Grav.* 38, 095002 (2021).
 - [47] J. M. Bardeen, W. H. Press, and S. A. Teukolsky, Rotating Black Holes: Locally Nonrotating Frames, Energy Extraction, and Scalar Synchrotron Radiation, *The Astrophysical Journal* 178, 347 (1972).
 - [48] L. C. Stein and N. Warburton, Location of the Last Stable Orbit in Kerr Spacetime, *Phys. Rev. D* 101, 064007 (2020).